

KOCH-LIKE SIDED SIERPINSKI GASKET MULTIFRACTAL DIPOLE ANTENNA

D. T. Li* and J. F. Mao

Key Laboratory of Ministry of Education of China for Research and Design of Electromagnetic, Compatibility of High Speed Electronic Systems, Shanghai Jiao Tong University, Shanghai 200240, China

Abstract—Koch-like fractal curve and Sierpinski Gasket are syncretized in minor-main way, forming so called Koch-like sided Sierpinski Gasket multifractal dipole (KSSG). Some iterative combinatorial cases of the two monofractals $\mathbf{K}_i\mathbf{S}_j$ KSSG have been investigated in free space without feedline for revealing the assumed multifractal property. Then a pragmatistical coplanar stripline (CPS) fed $\mathbf{K}_4\mathbf{S}_1$ KSSG multifractal bow-tie dipole with dimension of $61.1\text{ mm} \times 34.75\text{ mm}$ was designed, fabricated and measured. Six matched bands ($S_{11} < -10\text{ dB}$) with moderate gain (2 dBi–6 dBi) and high efficiency (80%–95%) are obtained within band 1.5 GHz–14 GHz, of which $\mathbf{f}_1 = 2.137\text{ GHz}$ (1.978–2.287 GHz, 309 MHz, 14.46%, PCS1900 + IMT2000 + UMTS), $\mathbf{f}_2 = 4.103\text{ GHz}$ (3.916–4.2 GHz, 374 MHz, 9.12%, WiMAX), $\mathbf{f}_3 = 5.596\text{ GHz}$ (5.499–5.679 GHz, 180 MHz, 3.22%, WLAN + WiMAX) are commonly used. Gain patterns of these bands are all almost omnidirectional in H -plane ($\mathbf{\Phi} = 0^\circ$, XOZ) and doughnut-shaped in E -plane ($\mathbf{\Phi} = 90^\circ$, YOZ), which suggests that $\mathbf{K}_4\mathbf{S}_1$ KSSG operates as a half-wavelength dipole. It behaviors like the main fractal in low frequency and resembles the minor one in high frequency. The consistent results of simulation and measurement have evinced the multifractal antennas' peculiar properties and superiority over its monofractals in impedance uniformity, gain pattern, efficiency and dimension. So it is attractive to PCS, UMTS, WLAN, Wi-Fi, WiMAX and other communication systems.

Received 4 January 2012, Accepted 1 March 2012, Scheduled 26 March 2012

* Corresponding author: Daotie Li (maplebirchpaeony@yahoo.com.cn).

1. INTRODUCTION

FRACTAL antenna has been investigated and commercialized over fifteen years since it was put forth by Nathan Cohen early in 1995 [1, 2]. It is a combination of antenna technology and fractal geometry [3]. Fractal antenna usually utilizes quasi-fractal or pre-fractal geometry which represents self-similarity, space-filling and repeats itself in finite different scales. The adjacent resonant frequency ratio is quite approximately equal to the fractal scale ratio [4–6]. It has shown many particular attributes during extensive researches and applications as concluded in [7, 8]. However, almost all contrived fractal antennas and previous fractal antenna studies have only focused upon monofractal geometry hereunto, which usually has single fractal scale ratio. Therefore, it is difficult to be utilized to design multiband antenna with several different resonant frequency ratios. This should be a great disadvantage of monofractal antenna. Naturally, we conceive the idea of fabricating multifractal antenna with several different fractal scale ratios so that we can design arbitrary multiband antenna more easily.

As we know, multifractal is a concept usually referred to Statistical Physics, Chemistry, Thermodynamics, and so on in Fractal Geometry [9]. Fractal dimension \mathbf{D} is used to describe the irregular trait of fractal, which often has only a single self-similar structure. Just as its name implies, multifractal has a continuous fractal dimension distribution. This distribution can be usually described with a fractal spectrum function $\mathbf{f}(\alpha)$ [10], which depicts the irregular fractal's properties of different scale and level. Multifractal has only referred to anomalous fractal, which is generally relevant to physical quantity such as quality, concentration, density, strength, and so forth. We know what's most closely interrelated with fractal antenna is shape fractal. Does shape multifractal exist? If it exists, is its fractal spectrum continuous or discrete? If the spectrum function is continuous, whether will the shape be so desultory that it cannot be constructed? And if it is discrete, whether should the shape be formed with several simple fractals? Multifractal has not been substantially explored for antenna design.

Like fractal antenna, design of multifractal antenna also begins with fractal shape construction. However, it is difficult to fabricate a multifractal geometry because it's hard to contrive different component fractals and piece them together. This could be one reason that there haven't been any multifractal antennas fabricated up to now. Therefore, we naturally attempt to form multifractal shape from well known monofractal, such as Koch Curve/Snowflake, Sierpinski

Gasket/Carpet, Minkowski Ring, and so on. We transform rectilinear sides of Sierpinski Gasket into Koch-like fractal curves then we obtain Koch-like sided Sierpinski Gasket multifractal. Here, we denote the multifractal as **KSSG** for simplicity. We will investigate various iterative combinations of the **KSSG** experimentally. At last, we chose **K₄S₁** as pragmatic antenna solutions for **KSSG**. After optimal design by simulation with Ansoft HFSSTM v.13, we fabricate and measure the physical **KSSG** dipole. The consistent good results between simulation and measurement reveal and validate the particularity and advantages of multifractal antenna in impedance uniformity, gain pattern, efficiency and dimension.

2. KOCH-LIKE SIDED SIERPINSKI GASKET (KSSG)

2.1. The Multifractal Geometry

This proposed multifractal derives from Sierpinski Gasket and Koch-like fractal curve. The two fractals were combined in superiority-inferiority order with individual iterative. Sierpinski forms the panorama and Koch-like fractal reforms the local sides. Here, a general designation **K_iS_j** (**K_i**-Koch-like, **S_j**-Sierpinski Gasket) is given to the two fractals for convenience. For acquisition of conspicuous multifractal traits, we choose iterative **S₁** and **K₄** for Sierpinski Gasket and Koch-like curve respectively. A **K₀-K₄** iterated Koch-like sided isosceles triangle replicates itself twice then the copies move to the base vertexes, forming the **S₁** iterated Koch-like sided Sierpinski Gasket (denoted as **K₀S₁-K₄S₁** **KSSG**), as shown in Fig. 7. Apparently, the base angle of Sierpinski Gasket is equal to that of Koch-like sided isosceles and their size ratio is 2 : 1.

Intuitively, performances of the multifractal antenna are intimately relevant to Koch-like fractal. Therefore, we will introduce this fractal briefly. It is fabricated from an isosceles triangle. A small isosceles triangle is cut off from centre of each side of the initial isosceles triangle, then the procedure iterates in the tips of two sides of each angle of the notched triangle while a smaller one protrudes from middle of equilateral sides of each isosceles-triangular notch of last iterative. The iterative procedure itself proceeds, forming the novel fractal bow-tie geometry, as shown in Figs. 1–6. The dipole is fully parameterized modeled and simulated with Ansoft HFSSTM v.13. The parameters' symbols and meanings are as follows: θ is base angle of the initial isosceles triangle, φ is base angle of each iterative isosceles-triangular notch, ν is rectilinear base side length of the isosceles dipole triangle, ι is half length of base side of the initial isosceles-triangular notch, α is the ratio of side length of initial *i*th iterated isosceles triangles

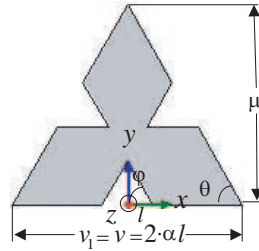
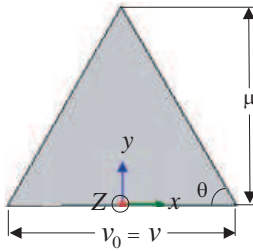


Figure 1. \mathbf{K}_0 , $\theta = 60^\circ$ $\nu = 19.56$ mm. **Figure 2.** \mathbf{K}_1 , $l = 2.31$ mm.

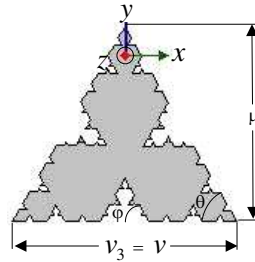
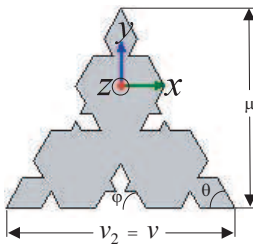


Figure 3. \mathbf{K}_2 , $l = 0.88$ mm. **Figure 4.** \mathbf{K}_3 , $l = 0.34$ mm.

to the base side length of $(i + 1)$ th $(i = 0, 1 \dots n)$ iterated isosceles notches of \mathbf{K}_n -iterated Koch-like sided isosceles triangle, as shown in Figs. 2 and 6, μ is height of the isosceles dipole triangle. There is a relationship among these arguments:

$$\nu = \frac{(2 \cdot \alpha)^n}{(\alpha - 1)^{n-1}} \cdot l_n \Leftrightarrow l_n = \frac{(\alpha - 1)}{2 \cdot \alpha} \cdot l_{n-1} = \chi^{n-1} l_1 \quad (n = 1, 2 \dots), \quad (1)$$

where ν_n is linear base side length of each iterative and $\nu_0 = \nu_1 = \nu_2 = \nu_3 = \nu_4 = \nu$. We choose $\theta = 60^\circ$, $\varphi = 60^\circ$, $\nu = 39.3$ mm, $\alpha = 4.25$, $\mu = 34$ mm for the iterative procedure.

Now we assume that \mathbf{S}_i , \mathbf{B}_i $(i = 0, 1, 2, 3, 4)$ are the lateral side length and base side length of the fractal isosceles triangle of each iterative respectively. The relationships between \mathbf{S}_i , \mathbf{B}_i and θ , φ , α , l can be expressed as formulas below.

$$\begin{aligned} \mathbf{S}_n &= \sigma^n \cdot (\alpha \cdot l_1 \cdot \sec \theta) = (\sec \theta \cdot \alpha \cdot \chi) \cdot (\sigma \cdot \chi^{-1})^n \cdot l_n; \\ \mathbf{B}_n &= \sigma^n \cdot (2 \cdot \alpha \cdot l_1) = (2 \cdot \alpha \cdot \chi) \cdot (\sigma \cdot \chi^{-1})^n \cdot l_n; \\ \sigma &= \frac{(\alpha - 1 + \sec \varphi)}{\alpha} \end{aligned} \quad (2)$$

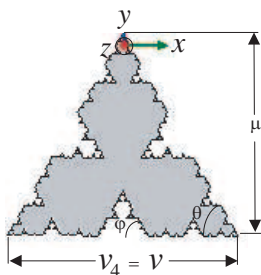


Figure 5. K_4 , $\iota = 0.13$ mm.



Figure 6. Koch-like curve.

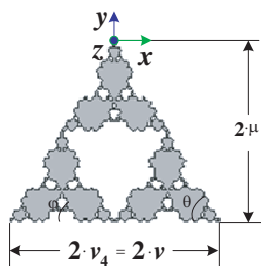


Figure 7. K_3S_1 KSSG.

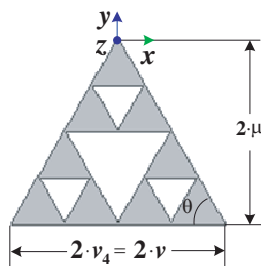


Figure 8. K_0S_2 Sierpinski Gasket.

According to the definition of box dimension of fractal geometry [8] and the formulas above, we can derive fractal dimension of the Koch-like fractal curve along the lateral sides and base side of the isosceles triangle as follows:

$$\begin{aligned}
 \mathbf{D} &= \lim_{\delta \rightarrow 0, N \rightarrow \infty} \frac{\log N(\delta)}{\log\left(\frac{1}{\delta}\right)} = \lim_{\delta \rightarrow 0, n \rightarrow \infty} \frac{\log\left(\frac{S_n}{l_n}\right)}{\log\left(\frac{1}{l_n}\right)} = \lim_{\delta \rightarrow 0, n \rightarrow \infty} \frac{\log\left(\frac{B_n}{l_n}\right)}{\log\left(\frac{1}{l_n}\right)} \\
 &= \lim_{\delta \rightarrow 0, n \rightarrow \infty} \left\{ \frac{\log\left[(\sec \theta \cdot \alpha \cdot \chi) \cdot (\sigma \cdot \chi^{-1})^n\right]}{\log\left(\frac{1}{\chi^{n-1} \cdot l_1}\right)} \right\} \approx 1 + \frac{\log \sigma}{\log \frac{1}{\chi}} \approx 1.2382 \quad (3)
 \end{aligned}$$

\mathbf{D} is very approximate to $\frac{\log 4}{\log 3}$, which is the fractal dimension of Von Koch Curve, because it is Koch-like. A special case for \mathbf{D} is: $\varphi = 60^\circ$, $\alpha = 3$, $\mathbf{D} = \frac{\log 4}{\log 3} \approx 1.2617$.

From formula (3), we know that \mathbf{D} increases with φ , α , ν and decreases with K_1 and is independent of θ and ι .

2.2. Simulation Results and Discussion

For validation of the supposition of the multifractal properties deriving from Koch-like sided isosceles triangle unit cell, we experiment on this inferior fractal Koch-like sided fractal bow-tie from iterative \mathbf{K}_0 to \mathbf{K}_4 with the superior \mathbf{S}_1 iterative Sierpinski Gasket within band 1 GHz–70 GHz. Incidentally, we explore the properties of equidimensional Sierpinski gasket dipole of each iterative. Then we compare $\mathbf{K}_1\mathbf{S}_1$ – $\mathbf{K}_4\mathbf{S}_1$ KSSG with $\mathbf{K}_0\mathbf{S}_0$ – $\mathbf{K}_0\mathbf{S}_4$ Sierpinski Gasket, as shown in Fig. 8, for further revelation of the advantages and peculiarity of the multifractal dipole. We merge the simulated reflection coefficients and radiation patterns of the resonant frequencies of each iterative $\mathbf{K}_0\mathbf{S}_1$ – $\mathbf{K}_4\mathbf{S}_1$ and $\mathbf{K}_0\mathbf{S}_0$ – $\mathbf{K}_0\mathbf{S}_4$ respectively for this purpose, as shown in Figs. 9–14.

Here, distinct multifractal idiosyncrasy is obtained from a set of optimal arguments of Koch-like fractal, which are yielded with vast experiments by mean of multiple Parametric Sweeps from Ansoft HFSSTM v.13 Optimetrics. The parameters are $\nu_0 = \nu_1 = \nu_2 = \nu_3 = \nu_4 = \nu = 19.56$ mm, $\mu = 17$ mm, $\theta = 60^\circ$, $\varphi = 60^\circ$, $\alpha = 3.125$, $\iota_1 = 3.136$ mm, $\iota_2 = 1.066$ mm, $\iota_3 = 0.3625$ mm, $\iota_4 = 0.12325$ mm. So the dimension of the multifractal Sierpinski Gasket dipole antenna is $4\mu \times 2\nu = 68$ mm \times 39.12 mm, as shown in Fig. 7. For good impedance match and current distribution [11], baselengths of the overlapped tips are chosen as: $2 \times \iota_4 = 0.2465$ mm. The dipole is fed at vertexes of this pair of Sierpinski gasket triangles at 50Ω in free space for experimental revelation of its multifractal traits.

First and foremost, we studied multifractal properties from input impedance $\mathbf{Z}_{in}(\mathbf{f}) = \mathbf{R}_{in}(\mathbf{f}) + \mathbf{j}\mathbf{X}_{in}(\mathbf{f})$ of each iterative, as shown in

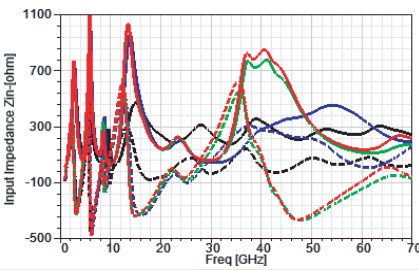


Figure 9. Input impedance $\mathbf{Z}_{in}(\mathbf{f})$ of $\mathbf{K}_i\mathbf{S}_1$ KSSG ($\mathbf{K}_1\mathbf{S}_1$ -black, $\mathbf{K}_2\mathbf{S}_1$ -blue, $\mathbf{K}_3\mathbf{S}_1$ -green, $\mathbf{K}_4\mathbf{S}_1$ -red; solid-real, dash-imaginary).

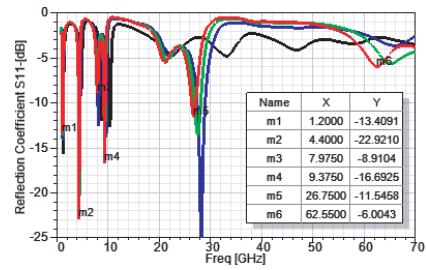


Figure 10. Reflection coefficients \mathbf{S}_{11} of $\mathbf{K}_i\mathbf{S}_1$ KSSG ($\mathbf{K}_1\mathbf{S}_1$ -black, $\mathbf{K}_2\mathbf{S}_1$ -blue, $\mathbf{K}_3\mathbf{S}_1$ -green, $\mathbf{K}_4\mathbf{S}_1$ -red).

Figs. 7, 22, and 24. We tabulate those frequencies and resistances corresponding to $\mathbf{X}_{in}(\mathbf{f}_i) \approx \mathbf{0}$ of $\mathbf{Z}_{in}(\mathbf{f})$ in Table 1.

As shown in Table 1, with increment of $\mathbf{K}_i\mathbf{S}_1$, resistances of $Z_{in}(\mathbf{f}_1)$, $Z_{in}(\mathbf{f}_2)$ decreases and $Z_{in}(\mathbf{f}_3)$ - $Z_{in}(\mathbf{f}_6)$ increases. Meanwhile, new resonant frequencies emerge in upper band as existent \mathbf{f}_i shift towards lower band with \mathbf{K}_i 's increment. The size is reduced by 11%–12.9% and 45.6% compared with the initiator and rectilinear bow-tie dipole. $\mathbf{K}_i\mathbf{S}_j$ KSSG has $(n = i + j + 1)$ matched bands [12]. $\mathbf{K}_i\mathbf{S}_1$ multifractal dipole present two impedance attractors, which are approximately centered around resistances 50Ω and 120Ω (underlined) respectively while its monofractal counterparts $\mathbf{K}_i\mathbf{S}_0$ takes on only one attractor and $\mathbf{K}_0\mathbf{S}_j$ has none, of which resistance continuously fluctuates between 40Ω and 140Ω . We feed the $\mathbf{K}_i\mathbf{S}_j$ dipole at 50Ω then tabulate its matched frequency \mathbf{f}_i , bandwidth and gain of each iterative also in Table 1.

Additionally, with increase of $\mathbf{K}_i\mathbf{S}_1$, gain pattern of \mathbf{f}_1 are almost invariable, as shown in Fig. 13(a); gain pattern of \mathbf{f}_2 increases by 0.4 dBi in Z -axis, as shown in Fig. 13(b); gain pattern of \mathbf{f}_3 observably ameliorates omni-directivity in H -plane, broadens main beamwidth in E -plane and gain increases by 2.48 dBi in Z -axis, as shown in Fig. 13(c); gain pattern of \mathbf{f}_4 transmutes from quatrefoiled shape to bifoiled shape in E -plane, significantly enhances omni-directivity in H -plane and gain increases drastically by 6.93 dBi in Z -axis, as shown in Fig. 13(d); gain pattern of \mathbf{f}_5 narrows its main beam in Z -axis but gain slightly decreases in this direction, as shown in Fig. 13(e); gain pattern of \mathbf{f}_6 meliorates omni-directivity in H -plane, reduces side lobe in E -plane and gain slightly decreases in Z -axis, as shown in Fig. 13(f). Meantime, absolute and relative bandwidths fall off

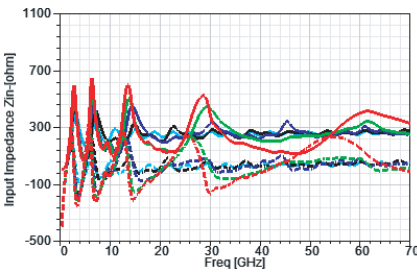


Figure 11. Input impedance $\mathbf{Z}_{in}(\mathbf{f})$ of $\mathbf{K}_0\mathbf{S}_j$ Sierpinski Gasket dipole ($\mathbf{K}_0\mathbf{S}_0$ -cyan, $\mathbf{K}_0\mathbf{S}_1$ -black, $\mathbf{K}_0\mathbf{S}_2$ -blue, $\mathbf{K}_0\mathbf{S}_3$ -green, $\mathbf{K}_0\mathbf{S}_4$ -red; solid-real, dash-imaginary)

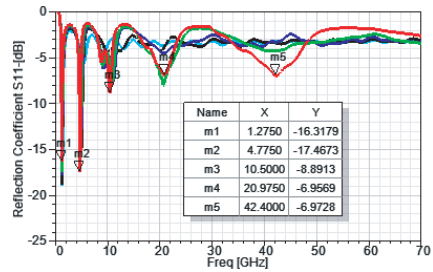


Figure 12. Reflection coefficients \mathbf{S}_{11} of $\mathbf{K}_0\mathbf{S}_j$ Sierpinski Gasket dipole ($\mathbf{K}_0\mathbf{S}_0$ -cyan, $\mathbf{K}_0\mathbf{S}_1$ -black, $\mathbf{K}_0\mathbf{S}_2$ -blue, $\mathbf{K}_0\mathbf{S}_3$ -green, $\mathbf{K}_0\mathbf{S}_4$ -red).

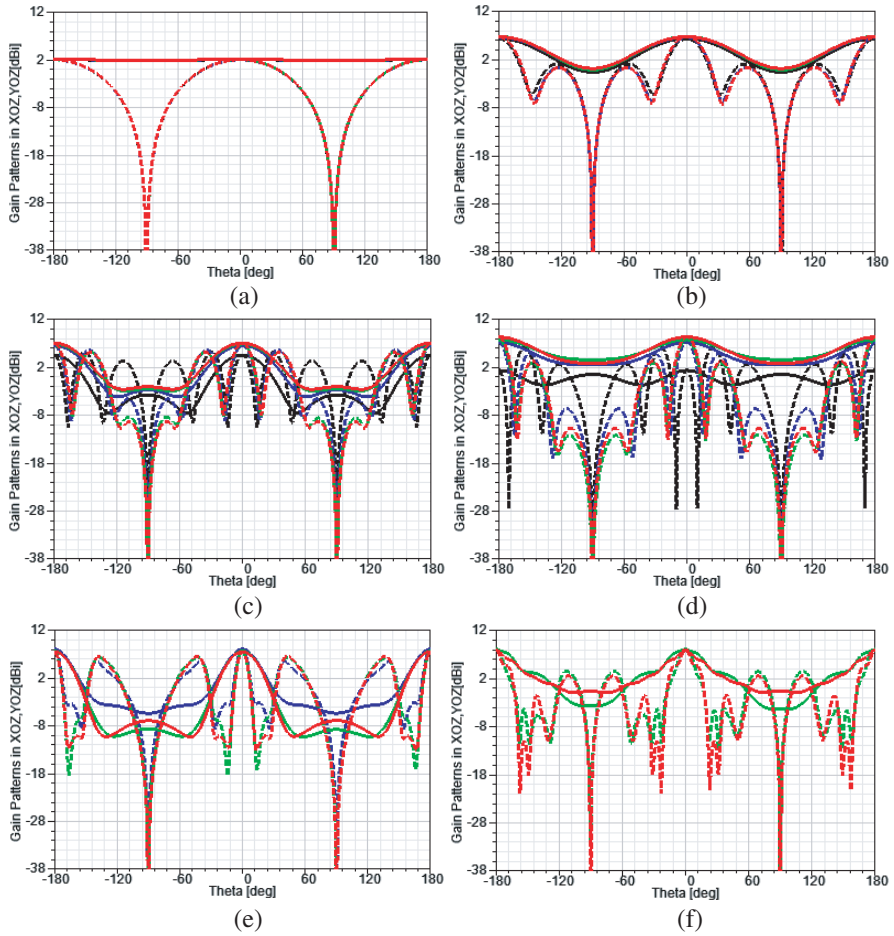


Figure 13. Gain patterns of $\mathbf{K}_i \mathbf{S}_1$ at \mathbf{f}_i ((a) \mathbf{f}_1 , (b) \mathbf{f}_2 , (c) \mathbf{f}_3 , (d) \mathbf{f}_4 , (e) \mathbf{f}_5 , (f) \mathbf{f}_6 ; solid- $\Phi = 0^\circ$, XOZ ; dash- $\Phi = 90^\circ$, YOZ ; $\mathbf{K}_1 \mathbf{S}_1$ -black, $\mathbf{K}_2 \mathbf{S}_1$ -blue, $\mathbf{K}_3 \mathbf{S}_1$ -green, $\mathbf{K}_4 \mathbf{S}_1$ -red, \mathbf{f}_i are shown in Table 1).

simultaneously. However, percentage bandwidths of newly emerging matched bands don't diminish with iterative probably because \mathbf{A}_i of \mathbf{KSSG} decreases with \mathbf{K}_i but infinitely approaches to a constant. Gain patterns of \mathbf{f}_1 - \mathbf{f}_6 are quasi-omnidirectional in H -plane (XOZ), but become cloven in E -plane (YOZ) except \mathbf{f}_1 . They peak at $\Theta = 0^\circ, \pm 180^\circ$ and null at $\Theta = \pm 90^\circ$, yielding one sidelobe ($\Theta = \pm 30^\circ - \pm 70^\circ, \pm 150^\circ - \pm 110^\circ$) in angular domain of $\Theta = 0^\circ - \pm 90^\circ, \pm 90^\circ - \pm 180^\circ$, as shown in Figs. 13(c)-(f), which indicate that $\mathbf{K}_i \mathbf{S}_1$ \mathbf{KSSG} is not half-wavelength dipole at these frequencies. And these

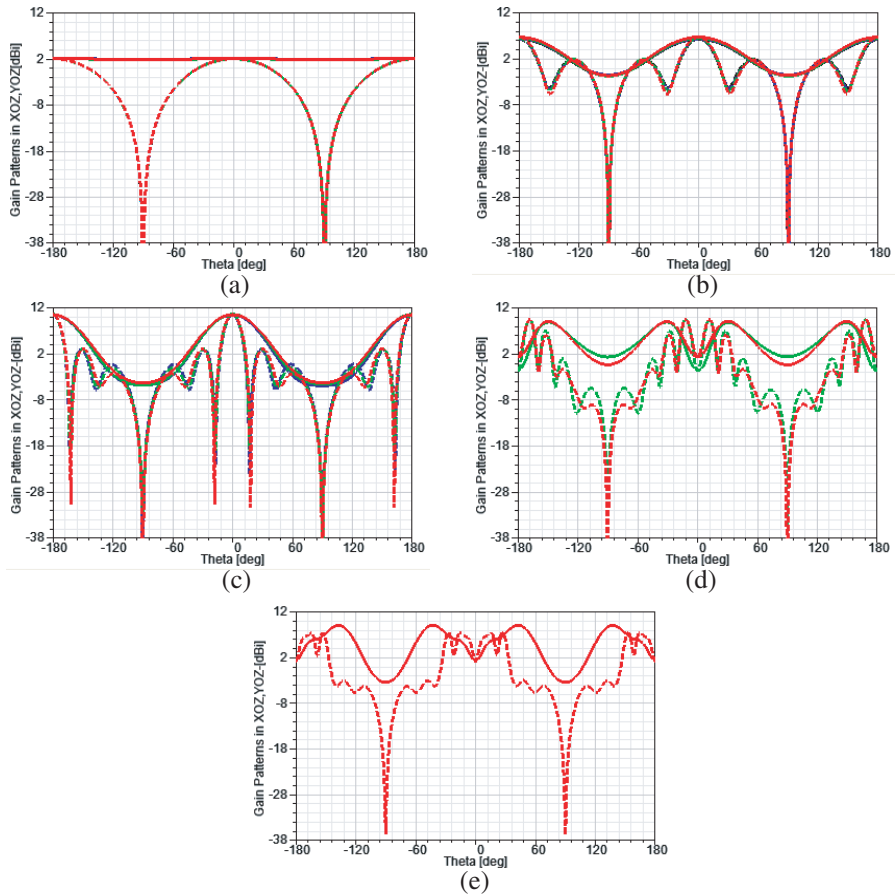


Figure 14. Gain patterns of $\mathbf{K}_0\mathbf{S}_j$ at \mathbf{f}_i ((a) \mathbf{f}_1 , (b) \mathbf{f}_2 , (c) \mathbf{f}_3 , (d) \mathbf{f}_4 , (e) \mathbf{f}_5 ; solid- $\Phi = 0^\circ$, XOZ ; dash- $\Phi = 90^\circ$, YOZ ; $\mathbf{K}_0\mathbf{S}_0$ -cyan, $\mathbf{K}_0\mathbf{S}_1$ -black, $\mathbf{K}_0\mathbf{S}_2$ -blue, $\mathbf{K}_0\mathbf{S}_3$ -green, $\mathbf{K}_0\mathbf{S}_4$ -red, as shown in Table 1).

gain patterns are very similar with that of Koch-like sided bow-tie dipole $\mathbf{K}_i\mathbf{S}_0$ and quite different from that of Sierpinski Gasket dipole $\mathbf{K}_0\mathbf{S}_j$ at \mathbf{f}_4 , \mathbf{f}_5 , as shown in Figs. 14(d)–(e).

From Fig. 10, we can see $\mathbf{K}_4\mathbf{S}_1$ KSSG shows marked multifractal reflection coefficient. Therefore, we illustrate surface current density distribution of resonant frequencies of this iterative case in Figs. 15–20. With the current distribution, we can intuitively unveils the multifractal trait in essence and better extrapolate the proportional relationships of adjacent resonant frequencies of each iterative case from Figs. 9, 10.

Table 1. Resistances, -8 dB BW and gain of each f_i of $K_i S_j$ (f_i -GHz, $R_{in} - \Omega$).

$K_i S_j$	f_i	f_1	f_2	f_3	f_4	f_5	f_6
$K_0 S_0$	f_i	1.35					
	R_{in}	40.1					
	BW (MHz)	300					
	G (dBi)	21.8%					
$K_0 S_1$	f_i	1.325	5.5				
	R_{in}	40.3	71.9				
	BW (MHz)	270,	475				
	G (dBi)	20%	9.3%				
$K_0 S_2$	f_i	1.325	4.985	11.085			
	R_{in}	40.5	78.4	115			
	BW (MHz)	253.6,	467,	—			
	G (dBi)	19.14%	9.37%				
$K_0 S_3$	f_i	1.30	4.90	10.875	20.75		
	R_{in}	39	72.2	115	148		
	BW (MHz)	238.4,	381,	—	—		
	G (dBi)	18.34%	7.78%				
$K_0 S_4$	f_i	1.275	4.775	10.575	20.975	42.40	
	R_{in}	37.4	67.2	107	128.6	128.2	
	BW (MHz)	219,	348,	336.2,	—	—	
	G (dBi)	17.18%	7.29%	3.1%			
$K_1 S_1$	f_i	1.25	4775	8.70	10.45		
	R_{in}	35.9	102	30.3	31.77		
	BW (MHz)	210,	200	350,	335,		
	G (dBi)	16.5%	4.2%	4.0%	3.2%		

	G (dBi)	1.95	6.24	4.43	1.24		
K₂S₁	f_i	1.225	4.525	8.15	9.675	28.225	
	R_{in}	34.9	71.1	79.0	33.3	51.1	
	BW (MHz)	180, 14.7%	280, 6.2%	3153.9%	260, 2.7%	2125, 7.6%	
	G (dBi)	1.95	6.53	6.47	7.07	7.92	
K₃S₁	f_i	1.2	4.425	7.95	9.475	27.525	65.20
	R_{in}	33.1	56.6	103.9	30.4	75.3	132.8
	BW (MHz)	160, 13.2%	270 6.1%	180 2.3%	265 2.8%	1750, 64%	—
	G (dBi)	1.96	6.63	6.75	7.65	7.93	7.93
K₄S₁	f_i	1.2	4.40	7.975	9.375	26.775	62.70
	R_{in}	33.1	577	104	37.6	834	146.4
	BW (MHz)	167, 13.9%	266 6.0%	186 2.4%	320 3.4%	1478, 5.5%	—
	G (dBi)	1.96	6.61	6.91	8.17	7.36	7.86

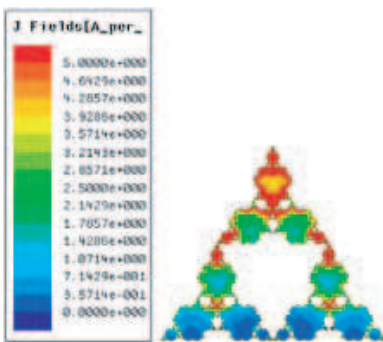


Figure 15. **K₄S₁** at **f₁** = 1.2 GHz.

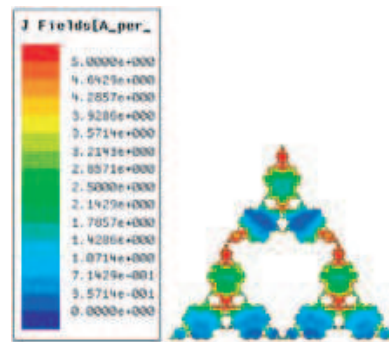


Figure 16. **K₄S₁** at **f₂** = 4.4 GHz.

As depicted in Fig. 15, current density \mathbf{J}_s maximizes at the vertexal feeding point and travels along the fractal equicrural sides to the base sides attenuating on and on, but boosts up at central discontinuities of each iterative. Along with the doughnut-shaped [13, 14] radiation pattern in E -plane, as shown in Fig. 13(a),

we can conclude that $\mathbf{K}_4\mathbf{S}_1$ operates as a half wavelength dipole at $\mathbf{f}_1 = 1.2\text{ GHz}$, so

$$\frac{\lambda_1}{4} \approx 2 \cdot \kappa_1 \cdot \mathbf{S}_4 + \varsigma_1 \cdot \mathbf{B}_4, \quad \varsigma_1 \rightarrow \mathbf{0}^+, \quad (4)$$

where $\varsigma_1 \rightarrow \mathbf{0}^+$ means λ_1 can propagate to the furthest and get cross the base vertexes. When $\mathbf{f}_2 = 4.4\text{ GHz}$, \mathbf{J}_s also maximizes at feeding point and augments at central joint discontinuities, but minimizes near base apexes of three isosceles triangle unit cells, so,

$$\frac{\lambda_2}{4} \approx \kappa_2 \cdot \mathbf{S}_4 + \varsigma_2 \cdot \mathbf{B}_4 (\kappa_2 \rightarrow \mathbf{1}^+, \varsigma_2 \rightarrow \mathbf{0}^+), \quad (5)$$

as depicted in Fig. 16. $\kappa_2 \rightarrow \mathbf{1}^+$ means λ_2 can only arrive to the proximal end away from the base vertexes of the upper isosceles triangle unit cell. For $\mathbf{f}_1 - \mathbf{f}_6$, \mathbf{J}_s also has this similar distribution property, but their corresponding wavelengths along the fractal lateral sides are shorten as:

$$\frac{\lambda_3}{4} \approx (\kappa_3 \cdot \chi) \cdot \mathbf{S}_4 (\kappa_3 \rightarrow \mathbf{1}^+) \quad (6)$$

$$\frac{\lambda_4}{4} \approx (\kappa_4 \cdot \chi) \cdot \mathbf{S}_4 (\kappa_4 \rightarrow \mathbf{1}^+) \quad (7)$$

$$\frac{\lambda_5}{4} \approx (\kappa_5 \cdot \chi^2) \cdot \mathbf{S}_4 (\kappa_5 \rightarrow \mathbf{1}^+) \quad (8)$$

$$\frac{\lambda_6}{4} \approx (\kappa_6 \cdot \chi^3) \cdot \mathbf{S}_4 (\kappa_6 \rightarrow \mathbf{1}^+) \quad (9)$$

respectively, which can be seen in Figs. 17–20. Formulas (5)–(9) indicate that adjacent frequency ratio δ is proportional to fractal scale ratio χ^{-1} in high frequency.

According to the analysis above, we can conclude that the $\mathbf{K}_i\mathbf{S}_j$ Koch-like sided Sierpinski Gasket dipole (**KSSG**) is a fire-new multifractal antenna and it doesn't operate as a half wavelength or a full wavelength dipole at resonant frequencies $\mathbf{f}_{\mathbf{n}\mathbf{j}}$ ($\mathbf{n} = \mathbf{f}_{\mathbf{n}}$; $\mathbf{i} - \mathbf{K}_i$) of its each iterative $\mathbf{K}_i\mathbf{S}_1$ besides \mathbf{f}_{1i} ($\mathbf{i} - \mathbf{K}_i\mathbf{S}_1$). We will deduce resonant frequency formulas for Sierpinski Gasket dipole $\mathbf{K}_0\mathbf{S}_1 - \mathbf{K}_0\mathbf{S}_4$ and **KSSG** multifractal dipole $\mathbf{K}_1\mathbf{S}_1 - \mathbf{K}_4\mathbf{S}_1$ respectively in the following section.

2.2.1. $\mathbf{K}_0\mathbf{S}_j$ (Sierpinski Gasket)

We have fabricated **KSSG** dipole on Sierpinski Gasket with Koch-like curve, so it's necessary to formulate the ratio of adjacent resonant frequencies of each iterative of Sierpinski Gasket counterpart. According to simulation results, as shown in Fig. 12 and empirical

knowledge, we proposed the formulas for Sierpinski Gasket dipole as follows.

$$\prod_{n=1}^{j+1} \beta_n^j \cdot (\gamma^j \cdot \mathbf{s}_0 + (1 - 0.04 \cdot \mathbf{j}) \cdot \xi \cdot \mathbf{b}_0) = \zeta_{nj}^1 \cdot \frac{\lambda_{nj}}{4} = \zeta_{nj}^1 \cdot \frac{c_0}{4 \cdot f_{nj}} \Rightarrow$$

$$f_{nj} = \frac{c_0}{4 \cdot \zeta_{nj}^{1-j} \cdot \prod_{n=1}^{j+1} \beta_n^j \cdot (\gamma^j \cdot \mathbf{s}_0 + (1 - 0.04 \cdot \mathbf{j}) \cdot \xi \cdot \mathbf{b}_0)}$$

$(\gamma = 1.04, \quad \xi = 0.4; \quad \beta_1^j = 1; \quad \beta_2^j = 0.2645, \quad \zeta_{nj}^1 = 1;$
 $\beta_3^j = 0.314 + 0.13 \cdot \sum_{k=2}^j 0.1^{k-2}, \beta_4^j = 0.365 + 0.15 \cdot \sum_{k=3}^j (-0.1)^{k-3};)$
 $\lim_{n \rightarrow j+1, j \rightarrow +\infty} \beta_n^j = 0.365 + 0.15 \cdot \sum_{k=3}^j (-0.1)^{k-3} = 0.5014 \approx 0.5$
 $(n = 1, 2 \dots j + 1; \quad j = 0, 1 \dots)$

Some symbols shown in formula (10) have their individual represents as follows: f_{nj} is the n th resonant frequency of S_j iterated Sierpinski Gasket dipole and total frequency number is $n = j + 1$, c_0 is speed of light in free space, \mathbf{s}_0 and \mathbf{b}_0 is lateral side length and base side length of the initial isosceles triangle respectively; ζ_{nj}^1 is multiplier of the quarter of wavelength, which denotes the dipole is half-wavelength ($\zeta_{ni}^1 = 1$) or full wave-length ($\zeta_{ni}^1 = 2$); γ is the ratio of EM wave's active propagating path and lateral side length of the initial bow-tie, and it is always somewhat larger than 1 ($\gamma = 1.04$);

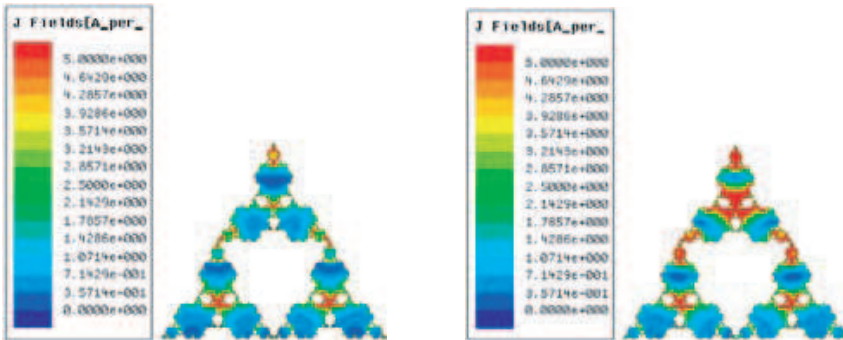


Figure 17. K_4S_1 at $f_3 = 9.775$ GHz. Figure 18. K_4S_1 at $f_4 = 9.375$ GHz.

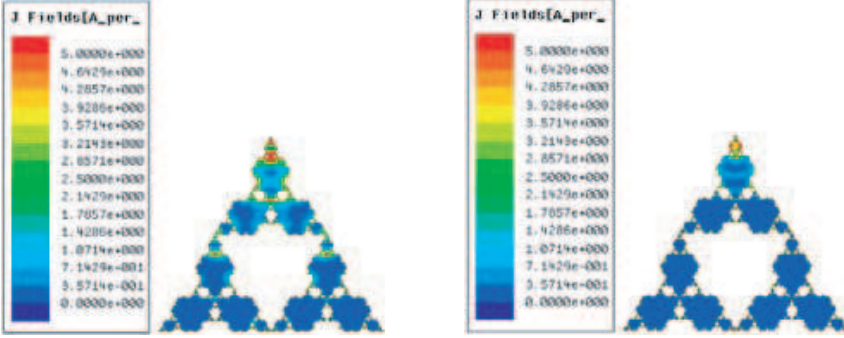


Figure 19. K_4S_1 at $f_5 = 26.775$ GHz. **Figure 20.** K_4S_1 at $f_6 = 62.7$ GHz.

ξ is the ratio of EM wave’s active propagating distance and base side length of the initial bow-tie because of its fringe or end effect [15], and it is always ratherish less than 0.5 ($\xi = 0.4$), which means that wave travels approaching to middle of the base side but never arrives there; β_n^j ($\beta_1^j = j$, $\beta_2^j = 0.264$) denotes the ratio of wavelength λ_{nj} of n th resonant frequency f_{nj} of each iterative case to lateral and base sides of the initial bow-tie, and its infinite case is very approximate to the geometrical scale factor of Sierpinski Gasket $\tau = 0.5$. Here, the author’s viewpoint that fractal antenna’s frequency ratio is quite close to its fractal scale factor $\delta = \chi^{-1}$ rather than its fractal dimension D is proven once again. What should be emphasized is that this rule is rigorously effective and accurate only when iterative number S_j is large enough, because fundamental resonant frequency f_1 is usually yielded by the overall geometry rather than fractal iterative process and significant parasitic phenomenon, such as fringe effect and coupling exists when S_j is small.

Hereunto, we have acquired the most important fractal electrical properties of superior Sierpinski Gasket fractal. Next, we will focus on inferior Koch-like fractal of the multifractal dipole.

2.2.2. K_iS_1 (KSSG)

Multifractal comprises different monofractals, which interrelate and interact with each other. When they are unified to form a brand-new multiple fractal, each individual will presents new traits, which is different from its original characters in isolated state. Therefore, $S_j = S_1$ is chosen here so that fractal electrical properties of Koch-like sided bow-tie will be better revealed because of less impact and

interference from the concomitant Sierpinski Gasket dominant fractal. \mathbf{K}_i iterated Koch-like side bow-tie has $\mathbf{n}_i = \mathbf{i} + 1$ resonant frequencies and \mathbf{S}_j iterated Sierpinski Gasket has $\mathbf{n}_j = \mathbf{i} + 1$ resonant frequencies, as shown in Fig. 10, so we can infer that $\mathbf{K}_i\mathbf{S}_j$ KSSG multifractal dipole should has $\mathbf{n}_{ij} = (\mathbf{i} + 1) + (\mathbf{j} + 1)$, $\mathbf{i} = 1, 2 \dots$ resonant frequencies in total. According to simulated results of $\mathbf{K}_i\mathbf{S}_1$ ($\mathbf{i} = 1, 2, 3, 4$), as depicted in Fig. 10 and formula (10), we deduce the proportional formula of contiguous resonant frequencies for the multifractal dipole as hereinafter.

$$\begin{aligned}
 & 2 \cdot \left(\prod_{n=1}^{i+3} \beta_{ni}^{j=1} \right) \cdot \sigma^{\log(1+0.45i)} \cdot (\mathbf{s}_0 + \varpi_{ni}^1 \cdot \mathbf{b}_0) = \zeta_{ni}^1 \cdot \frac{\lambda_{ni}}{4} = \frac{\zeta_{ni}^1 \cdot \mathbf{c}_0}{4 \cdot \mathbf{f}_{ni}} \Rightarrow \\
 & \mathbf{f}_{ni} = \frac{\mathbf{c}_0}{8 \cdot \zeta_{ni}^{-1} \cdot \left(\prod_{n=1}^{i+3} \beta_{ni}^1 \right) \cdot \sigma^{\log(1+0.45i)} \cdot \mathbf{b}_0 \cdot \left(\frac{1}{2 \cdot \cos \theta} + \varpi_{ni}^1 \right)} \\
 & (\zeta_{1i}^1 = 1, \quad \zeta_{ni}^1 = 2, \quad \mathbf{n} \geq 2; \\
 & \varpi_{1i}^1 = 0.25 - 0.02 \cdot \mathbf{i}, \quad \varpi_{2i}^1 = 0.129, \quad \varpi_{ni}^1 = 0 \quad (\mathbf{n} \geq 3); \\
 & \beta_{1i}^1 = 1.19; \quad \beta_{2i}^1 = 0.6926, \quad \beta_{3i}^1 = 1.2365 \cdot \chi, \quad \beta_{4i}^1 = 1.0587 \cdot \chi, \\
 & \beta_{5i}^1 = 1.0865 \cdot \chi^2, \quad \beta_{6i}^1 = 1.3583 \cdot \chi^3; \\
 & \lim_{\mathbf{n} \rightarrow \mathbf{i}+3, \mathbf{i} \rightarrow +\infty} \frac{\beta_{ni}^1}{\beta_{(n-1)i}^1} \approx \chi = \frac{\alpha - 1}{2 \cdot \alpha} \quad (\mathbf{n} = 1, 2 \dots \mathbf{i} + 3) \quad (11)
 \end{aligned}$$

According to the formula above, we find coefficients of formula (5)–(9) as follows:

$$\begin{aligned}
 \kappa_1 &= \beta_{14}^1 = 1.19, \quad \varsigma_1 = \beta_{14}^1 \cdot \varpi_{14}^1 = 0.2023; \\
 \kappa_2 &= \beta_{24}^1 = 0.6926, \quad \varsigma_2 = \beta_{24}^1 \cdot \varpi_{24}^1 = 0.0893; \\
 \kappa_3 &= \beta_{34}^1 = 1.2365, \quad \kappa_4 = \beta_{44}^1 = 1.0587; \\
 \kappa_5 &= \beta_{54}^1 = 1.0865, \quad \kappa_6 = \beta_{64}^1 = 1.3583;
 \end{aligned}$$

Some symbols in formula (11) have their individual represents as follows: \mathbf{f}_{nj} is the \mathbf{n} th resonant frequency of $\mathbf{K}_i\mathbf{S}_j$ KSSG multifractal dipole and the total frequency number is $\mathbf{n} = \mathbf{i} + 3$, $\mathbf{i} = 1, 2 \dots$; \mathbf{c}_0 , \mathbf{s}_0 and \mathbf{b}_0 are identical with those symbols defined in formula (10); σ is iterative side length ratio of Koch-like sided fractal bow-tie (physical scale ratio), as shown in formula (4); ζ_{ni}^1 is multiplier of the quarter of wavelength, which has identical definition with ζ_{ni}^1 in formula (10); ϖ_{ni}^1 also has the same definition with ξ in formula (10); β_{ni}^1 ($\beta_{1i}^1 = 1.19$; $\beta_{2i}^1 = 0.6926$, $\beta_{3i}^1 = 1.2365\chi$, $\beta_{4i}^1 = 1.0587\chi$, $\beta_{5i}^1 = 1.0865 \cdot \chi^2$, $\beta_{6i}^1 = 1.3583 \cdot \chi^3$) denotes the ratio of wavelength λ_{ni} of \mathbf{n} th resonant frequency \mathbf{f}_{nj} of each iterative \mathbf{i} and lateral and base sides of the initial

Table 2. Simulated $\mathbf{f}_{\mathbf{n}\mathbf{i}}^{\mathbf{j}}$ vs. calculated $\mathbf{f}_{\mathbf{n}\mathbf{i}}^{\mathbf{j}}$ of each iterative $\mathbf{K}_i\mathbf{S}_j$.

$\mathbf{K}_i\mathbf{S}_j$	\mathbf{f}_i (GHz)	\mathbf{f}_1	\mathbf{f}_2	\mathbf{f}_3	\mathbf{f}_4	\mathbf{f}_5	\mathbf{f}_6
$\mathbf{K}_0\mathbf{S}_0$	Cal	1.364					
	Sim	1.350					
$\mathbf{K}_0\mathbf{S}_1$	Cal	1.341	5.062				
	Sim	1.325	5.050				
$\mathbf{K}_0\mathbf{S}_2$	Cal	1.318	4.982	11.22			
	Sim	1.325	4.985	11.08			
$\mathbf{K}_0\mathbf{S}_3$	Cal	1.293	4.890	10.70	20.78		
	Sim	1.300	4.900	10.88	20.78		
$\mathbf{K}_0\mathbf{S}_4$	Cal	1.268	4.796	10.49	20.99	41.97	
	Sim	1.275	4.775	10.65	20.98	42.40	
$\mathbf{K}_1\mathbf{S}_1$	Cal	1.249	4.676	8.697	10.46		
	Sim	1.250	4.775	8.700	10.45		
$\mathbf{K}_2\mathbf{S}_1$	Cal	1.228	4.526	8.152	9.679	28.22	
	Sim	1.225	4.525	8.150	9.675	28.23	
$\mathbf{K}_3\mathbf{S}_1$	Cal	1.218	4.412	7.956	9.472	27.57	65.22
	Sim	1.200	4.425	7.950	9.475	27.53	65.20
$\mathbf{K}_4\mathbf{S}_1$	Cal	1.213	4.319	7.968	9.377	26.79	62.71
	Sim	1.200	4.400	7.975	9.375	26.78	62.70

(Note: **Cal**-calculated, **Sim**-simulated)

bow-tie unit cell, $\frac{\beta_{\mathbf{n}\mathbf{i}}^1}{\beta_{(\mathbf{n}-1)\mathbf{i}}^1} \approx \chi = \frac{\alpha-1}{2\cdot\alpha}$ indicates that $\mathbf{K}_i\mathbf{S}_1$ KSSG has an adjacent frequency ratio of which infinite case in high frequency band is very approximate to fractal scale factor of its inferior component monofractal Koch-like sided bow-tie $\delta = \chi^{-1} = \frac{2\cdot\alpha}{\alpha-1}$ rather than its fractal dimension \mathbf{D} ; $\sigma^{\log(1+0.45\cdot i)}$ denotes wavelength of $\mathbf{f}_{\mathbf{n}\mathbf{i}}$ is not equal to the fractal physical length $\sigma^i = (\frac{\alpha-1+\sec}{\alpha})^i$, so the frequency ratio of the multifractal dipole is not approximate to its physical length scale ratio σ but the fractal scale factor $\delta = \chi^{-1}$. Likewise, this rule is sufficiently accurate only when iterative number \mathbf{K}_i is large enough.

According to the formulas above, now we calculate $\mathbf{f}_{\mathbf{n}\mathbf{i}}$ and tabulate them with the simulated results for validation of our viewpoints in Table 2.

As shown in Table 2, the calculated $\mathbf{f}_{\mathbf{n}\mathbf{i}}^{\mathbf{j}}$ and the simulated $\mathbf{f}_{\mathbf{n}\mathbf{i}}^{\mathbf{j}}$ agree with each other well. Relative error between them is less than 1.5%. So, the formulas extrapolated for the resonant frequencies of $\mathbf{K}_i\mathbf{S}_j$ above are precise and more reasonable than that in [16, 17]. Heretofore, we can conclude that proportional coefficient δ of contiguous resonant

frequencies of the KSSG multifractal dipole is very approximate to fractal scale factor $\delta = \chi^{-1} = \frac{2\alpha}{\alpha-1}$ of Koch-like fractal in high frequency band rather than its fractal dimensions $\mathbf{D}_s = \mathbf{1} + \frac{\log \sigma}{\log \chi^{-1}} \approx 1.2382$ and physical scale ratio σ . In addition, $\zeta_{ni}^1 = 1, 2$ unveils that \mathbf{f}_{1i}^1 is half-wavelength and \mathbf{f}_{ni}^1 ($n \geq 2$) is full-wavelength. The radiation patterns shown in Fig. 25 can also prove this standpoint. Compared with $\mathbf{K}_0\mathbf{S}_j$ ($j = 1, 2 \dots$) and $\mathbf{K}_i\mathbf{S}_0$ ($i = 1, 2 \dots$), $\mathbf{K}_i\mathbf{S}_j$ ($i, j = 1, 2 \dots$) KSSG multifractal dipole has better \mathbf{S}_{11} in corresponding resonant frequencies than the former and has lower resonant frequencies in high frequency band than the latter.

The formulas (10) and (11) suggest that $\mathbf{K}_i\mathbf{S}_j$ present two stagger frequency ratios $\frac{f_{ni}^j}{f_{(n-1)i}^j} \approx 2$ and $\frac{f_{(n+1)i}^j}{f_{ni}^j} \approx \tau^{-1}$ only when n is approximate to $(i + j + 1)$ and i, j is large enough.

3. $\mathbf{K}_4\mathbf{S}_1$ KSSG MULTIFRACTAL DIPOLE ANTENNA

3.1. Physical Design of the Multifractal Dipole

$\mathbf{K}_i\mathbf{S}_1$ KSSG dipole manifests remarkable multifractal impedance property, significant size reduction and enhanced radiation patterns with Koch-like fractal's iterative i growing, as shown in Fig. 10, Table 1 and Figs. 9–15. Meanwhile, the fractal geometry gets more exquisite and complex as i increases. Thereupon, we have made a compromise between performances and complicity and we chose $\mathbf{K}_4\mathbf{S}_1$ as the physical antenna solution. For omni-directional radiation patterns in H -plane (XOZ), the pragmatic $\mathbf{K}_4\mathbf{S}_1$ multifractal antenna is designed as a dipole etched on Taconic TLY (tm) dielectric substrate with size of $75 \text{ mm} \times 60 \text{ mm} \times 1.0 \text{ mm}$ ($\mathbf{L} \times \mathbf{W} \times \mathbf{T}$, with $35 \mu\text{m}$ copper cladding), $\epsilon_r = 2.2$, and $\tan \delta = 0.0009$. We endowed the multifractal dipole with a set of optimum parameters yielded by optimization utilities Genetic Algorithm (GA) and Parametric Sweep of Ansoft HFSSTM v.13 Optimetrics as: $\theta = 60^\circ$, $\varphi = -45^\circ$, $\nu = 14.75 \text{ mm}$, $\alpha=1.8$, $\iota = 0.0485 \text{ mm}$, $\mathbf{L} = 61.1 \text{ mm}$, $\mathbf{W} = 29.5 \text{ mm}$. It is fed by 50Ω SMA connector through coplanar stripline (CPS) with dimension of $40 \text{ mm} \times 0.75 \text{ mm} \times 0.3 \text{ mm}$ ($\mathbf{L} \times \mathbf{W} \times \mathbf{G}$) at the vertexes of the upper Koch-like sided isosceles triangle unit cells, as shown in Fig. 21. The dipole prototype, as shown in Fig. 22 is fabricated by photolithprocess with a photolaser, which emits laser beam with facular diameter of $25 \mu\text{m}$. We measured \mathbf{S}_{11} with HP8722ES vector network analyzer within band 1.5 GHz–14 GHz, as shown in Fig. 24 (purple dash). Then we tested the radiation patterns in a commercial 3D anechoic chamber,

which is appropriate for measurement of mobile phone antenna and its upper frequency limit is about 7 GHz, so we can only measure f_1 , f_2 and f_3 , as shown in Figs. 25–30 (purple contours).

3.2. Advantages over the Monofractal Counterparts

In order to ulteriorly reveal the proposed multifractal antenna's superiority over monofractal one in performance, we choose its component fractals K_0S_1 Sierpinski Gasket and K_4S_0 Koch-like sided bow-tie as its comparative counterparts because the two fractal dipoles have most similar electrical properties with it. We model the monofractal dipoles identically with the proposed K_4S_1 KSSG

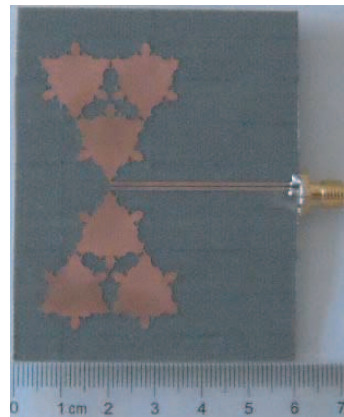
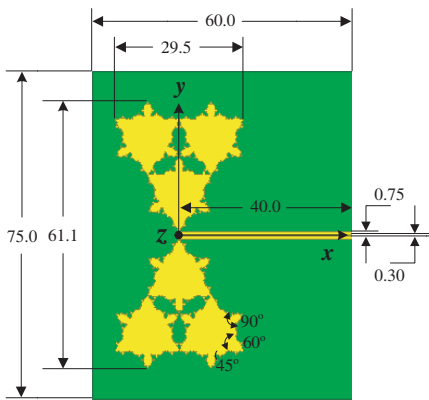


Figure 21. Geometry of K_4S_1 KSSG multifractal dipole (unit: mm).

Figure 22. Prototype of K_4S_1 KSSG multifractal dipole.

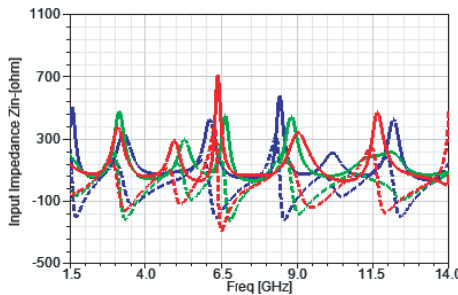


Figure 23. Input impedance Z_{in} (f) of K_iS_j (red-simulated K_4S_1 , green-simulated K_0S_1 , blue-simulated K_4S_0 ; solid- R_{in} , dash- X_{in}).

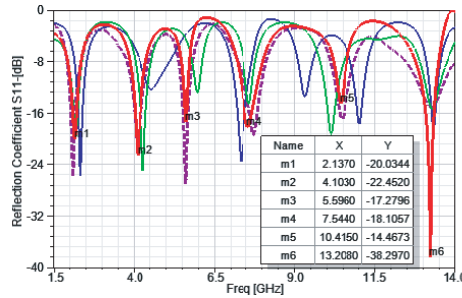


Figure 24. Reflection coefficient S_{11} of $K_i S_j$ (red solid-simulated $K_4 S_1$, purple dash-measured $K_4 S_1$, green solid-simulated $K_0 S_1$, blue solid-simulated $K_4 S_0$).

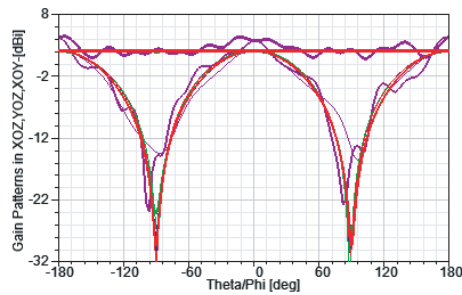


Figure 25. Gain patterns of $K_i S_j$ at f_1 (red- $f_1 = 2.137$ GHz-simulated $K_4 S_1$, purple- $f_1 = 2.078$ GHz-measured $K_4 S_1$, green- $f_1 = 2.17$ GHz- $K_0 S_1$, blue- $f_1 = 2.311$ GHz- $K_4 S_0$; bold- $\Phi = 0^\circ$ - XOZ , medium- $\Phi = 90^\circ$ - YOZ , thin- $\Theta = 90^\circ$ - XOY).

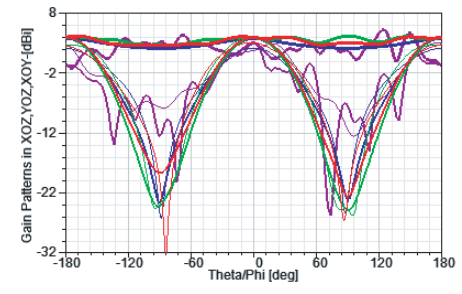


Figure 26. Gain patterns of $K_i S_j$ at f_2 (red- $f_2 = 4.1027$ GHz-simulated $K_4 S_1$, purple- $f_2 = 4.109$ GHz-measured $K_4 S_1$, green- $f_2 = 4.267$ GHz- $K_0 S_1$, blue- $f_2 = 4.528$ GHz- $K_4 S_0$; bold- $\Phi = 0^\circ$ - XOZ , medium- $\Phi = 90^\circ$ - YOZ , thin- $\Theta = 90^\circ$ - XOY).

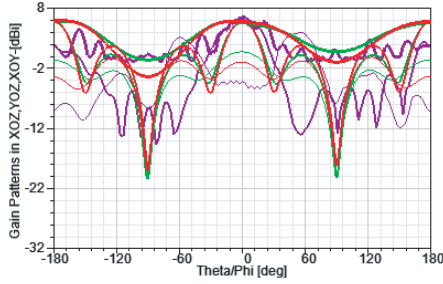


Figure 27. Gain patterns of $\mathbf{K}_1\mathbf{S}_j$ at f_3 (red- $f_3 = 5.596$ GHz-simulated $\mathbf{K}_4\mathbf{S}_1$, purple- $f_3 = 5.578$ GHz-measured $\mathbf{K}_4\mathbf{S}_1$, green- $f_3 = 5.947$ GHz- $\mathbf{K}_0\mathbf{S}_1$; bold- $\Phi = 0^\circ$ - XOZ , medium- $\Phi = 90^\circ$ - YOZ , thin- $\Theta = 90^\circ$ - XOY).

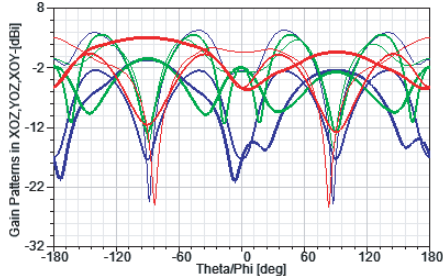


Figure 28. Gain patterns of $\mathbf{K}_1\mathbf{S}_j$ at f_4 (red- $f_4 = 7.546$ GHz-simulated $\mathbf{K}_4\mathbf{S}_1$, green- $f_4 = 7.576$ GHz- $\mathbf{K}_0\mathbf{S}_1$, blue- $f_3 = 7.304$ GHz- $\mathbf{K}_4\mathbf{S}_0$; bold- $\Phi = 0^\circ$ - XOZ , medium- $\Phi = 90^\circ$ - YOZ , thin- $\Theta = 90^\circ$ - XOY).

multifractal dipole, as shown in Fig. 21 and simulate them with the same software analysis setups. The simulated and measured results of $\mathbf{K}_4\mathbf{S}_1$ KSSG dipole and simulated results of $\mathbf{K}_0\mathbf{S}_1$ and $\mathbf{K}_4\mathbf{S}_0$ dipoles are merged into corresponding plots for discrepancy comparison and redundancy avoidance, as shown in Figs. 23–30.

As shown in Fig. 24, the reflection coefficient curves of $\mathbf{K}_4\mathbf{S}_1$, $\mathbf{K}_0\mathbf{S}_1$ and $\mathbf{K}_4\mathbf{S}_0$ seem as if they all have six true or dummy resonant frequencies corresponding to $S_{11} \leq -10$ dB within band 1.5 GHz–14 GHz. But only $\mathbf{K}_4\mathbf{S}_1$ has six true resonant frequencies corresponding to $S_{11} \leq -14$ dB and each f_{n4}^1 is lower than that of $\mathbf{K}_0\mathbf{S}_1$ and $\mathbf{K}_4\mathbf{S}_0$ except f_{54}^1 . Distinctly, $\mathbf{K}_1\mathbf{S}_j$ KSSG multifractal dipole has more uniform and consistent impedance property and further size reduction than its component monofractal counterparts $\mathbf{K}_0\mathbf{S}_j$ and $\mathbf{K}_i\mathbf{S}_0$. Also as shown in Fig. 24, measured S_{11} (purple dash) and

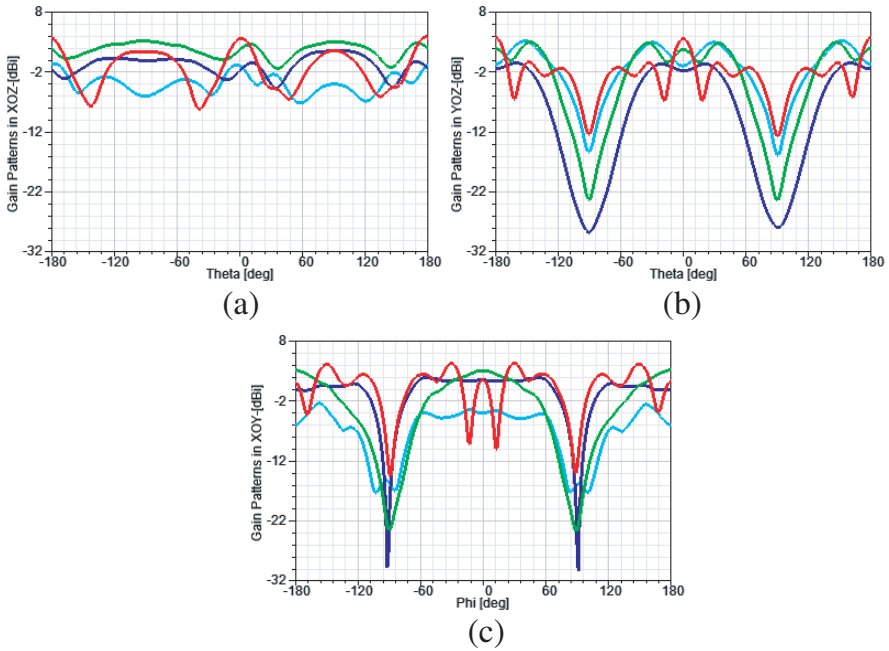


Figure 29. Gain patterns of $\mathbf{K}_i\mathbf{S}_j$ at \mathbf{f}_5 (red- $\mathbf{f}_5 = 10.415$ GHz-simulated $\mathbf{K}_4\mathbf{S}_1$, green- $\mathbf{f}_5 = 10.108$ GHz- $\mathbf{K}_0\mathbf{S}_1$, blue- $\mathbf{f}_4 = 9.3$ GHz- $\mathbf{K}_4\mathbf{S}_0$, cyan- $\mathbf{f}_5 = 11.004$ GHz- $\mathbf{K}_4\mathbf{S}_0$). (a) $\mathbf{Phi} = 0^\circ$ - \mathbf{XOZ} . (b) $\mathbf{Phi} = 90^\circ$ - \mathbf{YOZ} . (c) $\mathbf{Theta} = 90^\circ$ - \mathbf{XOY} .

simulated \mathbf{S}_{11} of $\mathbf{K}_4\mathbf{S}_1$ KSSG (red solid) agree well with each other though the former shows smaller values and slight upper shifting at all resonant frequencies. This could be mainly imputed to large ohmic loss of CPS and copper cladding in high frequency, substrate dielectric permittivity ϵ_r declination, fabrication tolerance and inherent error of the measurement systems.

Next, we will show radiation patterns of those frequencies \mathbf{f}_{ni}^j of $\mathbf{K}_i\mathbf{S}_j$, which are adjacent to each other in \mathbf{S}_{11} curves, as shown in Fig. 24, in one rectangular plot for comparison, as depicted in Figs. 25–30. In these plots, boldface, medium, lightface represents $\mathbf{Phi} = 0^\circ$, $\mathbf{Phi} = 90^\circ$, $\mathbf{Theta} = 90^\circ$ principle cut-plane respectively and red, purple, green, blue denote simulated and measured $\mathbf{K}_4\mathbf{S}_1$, $\mathbf{K}_0\mathbf{S}_1$, $\mathbf{K}_4\mathbf{S}_0$ in sequence. For distinct display of these patterns, adaptive dynamic range is chosen for these plots, as shown in Fig. 30.

Gain patterns of $\mathbf{K}_i\mathbf{S}_j$ KSSG at \mathbf{f}_1 and \mathbf{f}_2 are omnidirectional in \mathbf{XOZ} ($\mathbf{Phi} = 0^\circ$, \mathbf{H} -plane) and doughnut-shaped in \mathbf{YOZ} ($\mathbf{Phi} = 90^\circ$, \mathbf{E} -plane) and \mathbf{XOY} ($\mathbf{Theta} = 90^\circ$), as depicted in Figs. 25, 26. Gain patterns of $\mathbf{K}_4\mathbf{S}_1$ and $\mathbf{K}_0\mathbf{S}_1$ at \mathbf{f}_3 are also very alike, which are

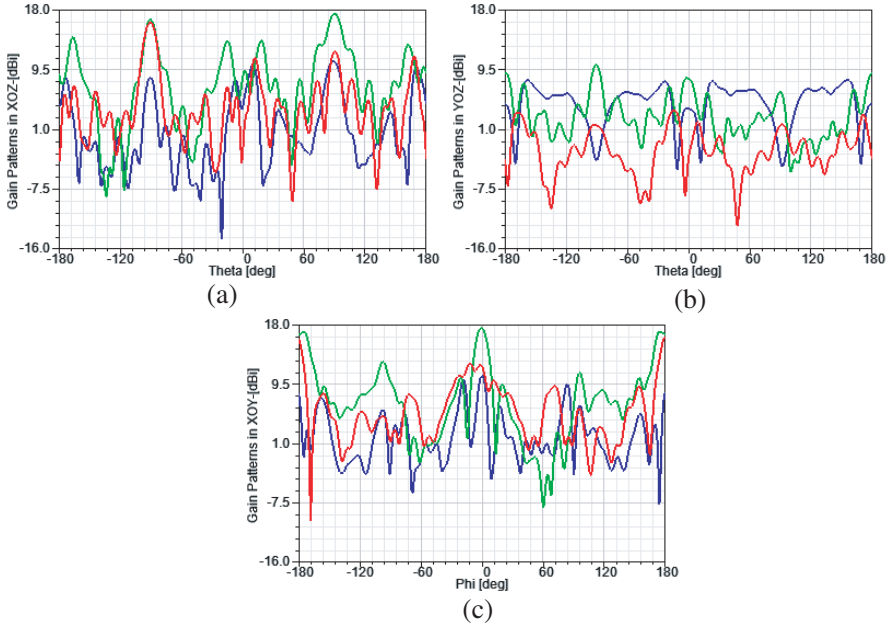


Figure 30. Gain patterns of $\mathbf{K}_i \mathbf{S}_j$ at \mathbf{f}_6 (red – $\mathbf{f}_6 = 13.208$ GHz-simulated- $\mathbf{K}_4 \mathbf{S}_1$, green- $\mathbf{f}_6 = 13.262$ GHz- $\mathbf{K}_0 \mathbf{S}_1$, blue- $\mathbf{f}_6 = 13.301$ GHz- $\mathbf{K}_4 \mathbf{S}_0$). (a) $\mathbf{Phi} = 0^\circ$ - XOZ . (b) $\mathbf{Phi} = 90^\circ$ - YOZ . (c) $\mathbf{Theta} = 90^\circ$ - XOY .

quasi-omnidirectional in XOZ ($\mathbf{Phi} = 0^\circ$, H -plane), cloven doughnut-shaped in YOZ ($\mathbf{Phi} = 90^\circ$, E -plane) and doughnut-shaped in XOY ($\mathbf{Theta} = 90^\circ$). $\mathbf{K}_4 \mathbf{S}_1$ and $\mathbf{K}_4 \mathbf{S}_0$ are quasi-omnidirectional, doughnut-shaped in XOZ ($\mathbf{Phi} = 0^\circ$, H -plane), dented doughnut-shaped, quatrefoil-shaped in YOZ ($\mathbf{Phi} = 90^\circ$) and dented doughnut-shaped in XOY ($\mathbf{Theta} = 90^\circ$, E -plane) at \mathbf{f}_4 and \mathbf{f}_3 respectively while $\mathbf{K}_0 \mathbf{S}_1$ is quatrefoil-shaped in XOZ ($\mathbf{Phi} = 0^\circ$, H -plane), cloven doughnut-shaped in YOZ ($\mathbf{Phi} = 90^\circ$, E -plane) and dented doughnut-shaped in XOY ($\mathbf{Theta} = 90^\circ$) at \mathbf{f}_4 , as depicted in Fig. 28. $\mathbf{K}_4 \mathbf{S}_1$, $\mathbf{K}_0 \mathbf{S}_1$ and $\mathbf{K}_4 \mathbf{S}_0$ are quatrefoil-shaped, quasi-omnidirectional in XOZ ($\mathbf{Phi} = 0^\circ$, H -plane), clove doughnut-shaped, dented doughnut-shaped in YOZ ($\mathbf{Phi} = 90^\circ$, E -plane) and cloven doughnut-shaped, doughnut-shaped in XOY ($\mathbf{Theta} = 90^\circ$, E -plane for $\mathbf{K}_4 \mathbf{S}_0$ at \mathbf{f}_5) at \mathbf{f}_4 and \mathbf{f}_4 , \mathbf{f}_5 respectively, as depicted in Fig. 29. Gain patterns of $\mathbf{K}_4 \mathbf{S}_1$ are multi-peaked and multi-null, which resemble that of both $\mathbf{K}_0 \mathbf{S}_1$ and $\mathbf{K}_4 \mathbf{S}_0$ at \mathbf{f}_6 , as shown in Fig. 30. Gain patterns of $\mathbf{K}_4 \mathbf{S}_1$ are more like that of $\mathbf{K}_0 \mathbf{S}_1$ at low frequencies \mathbf{f}_1 , \mathbf{f}_2 , \mathbf{f}_3 and high frequency \mathbf{f}_6 and more resemble that of $\mathbf{K}_4 \mathbf{S}_0$ at medium frequencies \mathbf{f}_4 , \mathbf{f}_5 .

Those radiation properties of $\mathbf{K}_4\mathbf{S}_1$ above corroborate the intuitive supposition that electromagnetic wave of different wavelength utilizes the main geometry and its vertexal Koch-like sided fractal region in low and high frequency respectively, so it both behaves like its main mono-fractal $\mathbf{K}_0\mathbf{S}_1$ and minor mono-fractal $\mathbf{K}_4\mathbf{S}_0$.

Measured gain patterns of \mathbf{f}_1 , \mathbf{f}_2 and \mathbf{f}_3 agree well with the simulated results, as shown in Figs. 25–27. The measured radiation efficiency of \mathbf{f}_1 , \mathbf{f}_2 and \mathbf{f}_3 is tabulated in Table 3.

Measured results show that the maximum radiations are in the vicinity of the normal direction and the radiation efficiency η decreases with \mathbf{f} , because loss increases in high frequency. The measured gain patterns are very approximate to the simulated gain patterns but have higher gain values. The $\mathbf{K}_4\mathbf{S}_1$ KSSG doesn't degrade in performance like bandwidth, gain and efficiency as the conclusions drawn for Koch monopole in [18]. At the end, we tabulate the comprehensive electrical properties of the $\mathbf{K}_i\mathbf{S}_j$ dipole for summary in Table 4.

As shown in Table 4, $\mathbf{K}_4\mathbf{S}_1$ KSSG also has more uniform input impedances than $\mathbf{K}_0\mathbf{S}_1$ and $\mathbf{K}_4\mathbf{S}_0$ just as it does in free space without feedline. $\mathbf{K}_4\mathbf{S}_1$, $\mathbf{K}_0\mathbf{S}_1$ and $\mathbf{K}_4\mathbf{S}_0$ have almost the same gains at \mathbf{f}_1 , but $\mathbf{K}_4\mathbf{S}_1$ is 0.06 dBi, 0.1 dBi and 0.39 dBi, 6.48 dBi higher at \mathbf{f}_2 and \mathbf{f}_3 than $\mathbf{K}_0\mathbf{S}_4$ and $\mathbf{K}_4\mathbf{S}_0$ respectively. E -plane transfers from YOZ in low frequency to XOY in high frequency because of existence of the CPS feedline. Likewise, the frequency ratio δ decreases with \mathbf{f} from 3.67 in free space without feeding to 1.245 of physical case also owing to existence of the CPS feedline. We will extrapolate formulas of operating frequency and adjacent frequency ratio later on. The $\mathbf{K}_4\mathbf{S}_1$ KSSG multifractal dipole has six matched bands for $S_{11} \leq -14$ dB within band 1.5 GHz–14 GHz, though only three

Table 3. Measured gain and efficiency of \mathbf{f}_1 , \mathbf{f}_2 and \mathbf{f}_3 (E , H -plane).

\mathbf{f}	Gain (E, dBi)	HPBW (E, °)	Gain (H, dBi)	HPBW (H, °)	Efficiency (η)
2.08	4.27	18	4.17	—	95.66%
2.12	4.05	26	4.05	—	95.15%
2.16	3.57	24	3.29	—	93.54%
3.85	4.31	16	2.91	—	83.78%
3.9	4.76	13	3.13	—	86.06%
3.95	4.56	14	2.93	—	88.57%
5.55	5.82	10.8	2.29	11	82.53%
5.60	5.68	10.5	2.48	11	81.97%
5.65	5.74	10.5	2.54	11	80.49%

Table 4. Simulated resonant properties and gain of $\mathbf{K}_i\mathbf{S}_j$ (+ \mathbf{Z} -axis).

$\mathbf{K}_4\mathbf{S}_1$	f_i (GHz)	f_1 2.137	f_2 4.103	f_3 5.596	f_4 7.546	f_5 10.415	f_6 13.208
	R_{in} (Ω)	76.52	60.52	38.3	68.58	34.38	52.17
	S_{11} (dB)	-20.3	22.45	17.28	18.11	14.47	38.30
	BW (MHz)	309,	374	180	647	282,	543
		14.46%	9.12%	3.22%	8.58%	2.71%	4.11%
	Gain (dBi)	2.09	4.12	5.85	3.0	3.8	16.20
$\mathbf{K}_0\mathbf{S}_1$	f_i (GHz)	f_1 2.17	f_2 4.267	f_3 5.947	f_4 7.576	f_5 10.108	f_6 13.262
	R_{in} (Ω)	61.36	44.63	79.56	34.18	62.31	70.74
	S_{11} (dB)	19.60	24.92	-12.811	-14.52	19.17	-15.30
	BW (MHz)	313,	373,	196	265	536	600
		14.42%	8.74%	3.94%	3.5%	5.31%	4.52%
	Gain (dBi)	2.14	4.06	5.75	2.70	3.1	17.45
$\mathbf{K}_4\mathbf{S}_0$	f_i (GHz)	f_1 2.311	f_2 4.528	f_3 7.304	f_4 9.3	f_5 11.004	f_6 13.301
	R_{in} (Ω)	53.74	77.48	53.48	72.94	66.93	38.09
	S_{11} (dB)	25.695	-12.28	-23.49	13.46	17.67	-18.615
	BW (MHz)	284,	548	540	296	394	323
		12.29%	12.1%	7.39%	3.18%	3.58%	2.43%
	Gain (dBi)	2.06	3.73	0.63	1.82	-0.65	10.63

of them are commonly used: $f_1 = 2.137$ GHz (1.978 GHz–2.287 GHz, 309 MHz, 14.46%, **PCS1900+UMTS+IMT-2000**), $f_2 = 4.103$ GHz (3.916 GHz–4.29 GHz, 374 MHz, 9.12%, **WiMAX**), $f_3 = 5.596$ GHz (5.499 GHz–5.679 GHz, 180 MHz, 3.22%, **WLAN + WiMAX**).

We assumed that $\mathbf{K}_i\mathbf{S}_1$ **KSSG** operates as a ζ_{ni}^g times half-wavelength dipole with half arm length of \mathbf{L}_{arm} . Instinctively, \mathbf{L}_{arm} comprises some fractal side length of $\mathbf{K}_i\mathbf{S}_1$ and a part of $\mathbf{L}_{CPS} - \mathbf{l}_{CPS} =$

3.2 mm (CPS width, gap and CPS–Bow-tie joint segment), we can derive the following formulas.

$$2 \cdot L_{\text{arm}} = \zeta_{\text{ni}}^g \cdot \frac{\lambda_{\text{ni}}^g}{2} = \zeta_{\text{ni}}^g \cdot \frac{\lambda_{\text{ni}}^0}{2\sqrt{\epsilon_r}} = \frac{\zeta_{\text{ni}}^g}{\sqrt{\epsilon_r}} \cdot \frac{\lambda_{\text{ni}}^0}{2} \quad (12)$$

$$L_{\text{arm}} = l_{\text{CPS}} + (\gamma_{\text{ni}}^1 \cdot S_{\text{ni}} + \varpi_{\text{ni}}^1 \cdot B_{\text{ni}}) \quad (13)$$

$$\begin{aligned} f_{\text{ni}}^1 &= \frac{\nu}{\lambda_{\text{ni}}^g} = \frac{c_0}{\sqrt{\epsilon_r} \lambda_{\text{ni}}^g} = \frac{c_0}{\lambda_{\text{ni}}^0} = \frac{c_0}{4 \cdot \left(\frac{\zeta_{\text{ni}}^g}{\sqrt{\epsilon_r}}\right)^{-1} \cdot [l_{\text{CPS}} + (\gamma_{\text{ni}}^1 \cdot S_{\text{ni}} + \varpi_{\text{ni}}^1 \cdot B_{\text{ni}})]} \\ &= \frac{c_0}{4 \cdot \left(\frac{\zeta_{\text{ni}}^g}{\sqrt{\epsilon_r}}\right)^{-1} \cdot \left[l_{\text{CPS}} + \left(\beta_{\text{ni}}^1 \cdot \chi \frac{\Psi_{\text{ni}}^1 - 1}{\sqrt{\epsilon_r}} \right) \cdot \sigma^i \cdot B_0 \cdot \left(\gamma_{\text{ni}}^1 \cdot \frac{1}{2\cos\theta} + \varpi_{\text{ni}}^1 \right) \right]} \end{aligned} \quad (14)$$

$$\begin{aligned} (l_{\text{CPS}} = 3.2 \text{ mm}; \quad \zeta_{\text{ni}}^g = 1, \quad \varpi_{\text{ni}}^1 = 0, \quad \gamma_{1i}^1 = 2, \quad \gamma_{\text{ni}}^1 = 1; \\ \mathbf{n} = 2, 3 \dots [1 + \mathbf{i} \cdot \sqrt{\epsilon_r}]_{\text{m}}; \quad \beta_{1i}^1 = 0.611, \quad \beta_{2i}^1 = 0.542, \\ \beta_{3i}^1 = 0.92, \quad \beta_{4i}^1 = 1.47, \quad \beta_{5i}^1 = 0.672, \quad \beta_{6i}^1 = 0.615; \\ \Psi_{1i}^1 = \Psi_{2i}^1 = 1; \quad \Psi_{3i}^1 = 2; \quad \Psi_{4i}^1 = \Psi_{5i}^1 = 3; \quad \Psi_{1i}^1 = 4; \quad \Psi_{\text{ni}}^1 = [1 + \mathbf{i} \cdot \sqrt{\epsilon_r}]_{\text{m}}) \end{aligned}$$

According to formulas (13) and (14), we get adjacent frequency ratio:

$$\delta_{\text{ni}} = \frac{\left[l_{\text{CPS}} + \left(\beta_{\text{ni}}^1 \cdot \chi \frac{\Psi_{\text{ni}}^1 - 1}{\sqrt{\epsilon_r}} \right) \cdot \sigma^i \cdot B_0 \cdot \left(\gamma_{\text{ni}}^1 \cdot \frac{1}{2\cos\theta} + \varpi_{\text{ni}}^1 \right) \right]}{\left[l_{\text{CPS}} + \left(\beta_{(\mathbf{n}+1)i}^1 \cdot \chi \frac{\Psi_{(\mathbf{n}+1)i}^1 - 1}{\sqrt{\epsilon_r}} \right) \cdot \sigma^i \cdot B_0 \cdot \left(\gamma_{(\mathbf{n}+1)i}^1 \cdot \frac{1}{2\cos\theta} + \varpi_{(\mathbf{n}+1)i}^1 \right) \right]}, \quad (15)$$

in which \mathbf{v} is velocity of wave in substrate, λ_{ni}^g , λ_{ni}^0 are wavelength of f_{ni}^1 in substrate and free space respectively, ζ_{n4}^1 ($= 1, 2 \dots \mathbf{n}$) is coefficient of half-wavelength, which has similar definition with ζ_{nj}^1 and ζ_{ni}^1 in formula (13) and (14), here $\zeta_{n4}^1 = 1$ denotes $\mathbf{K}_4\mathbf{S}_1$ KSSG operates as a half-wavelength dipole, $\gamma_{\text{ni}}^1 = 1, 2$ is number of isosceles unit cell got across by λ_{ni}^g and S_{ni} is its corresponding length on the lateral side, ϖ_{ni}^1 , B_{ni} is the proportional coefficient of length of λ_{ni}^g on base side and its overall length in several and $\varpi_{\text{ni}}^1 = 0$ means that end or fringe field is infinitesimal on base sides, $B_0 = 14.75 \text{ mm}$ is base side length of the isosceles triangle unit cell, $L_{\text{CPS}} = 40 \text{ mm}$ is the length of the CPS feedline, $\Psi_{\text{ni}}^1 = [1 + \mathbf{i} \cdot \sqrt{\epsilon_r}]_{\text{m}}$ denotes ceiling integer exponent of fractal scale ratio χ and β_{ni}^1 is its coefficient. The extrapolated formulas above for $\mathbf{K}_4\mathbf{S}_1$ KSSG are also applicable to its monofractal counterpart $\mathbf{K}_4\mathbf{S}_0$ but the arguments should have another

Table 5. Calculated \mathbf{f}_{ni}^1 and frequency ratio δ_{ni}^1 of $\mathbf{K}_4\mathbf{S}_1$.

\mathbf{f}_i (GHz)	\mathbf{f}_1	\mathbf{f}_2	\mathbf{f}_3	\mathbf{f}_4	\mathbf{f}_5	\mathbf{f}_6
Sim	2.137	4.103	5.596	7.546	10.415	13.208
Cal	2.03	4.112	5.614	7.542	10.461	13.185
δ_n	–	2.026	1.365	1.343	1.387	1.261

(Note: **Sim**-simulated, **Cal**-calculated)

set of appropriate values as follows:

$$\begin{aligned}
 & (\mathbf{B}_0 = 29.5 \text{ mm}; \zeta_{ni}^g = 1, \varpi_{ni}^1 = 0, \gamma_{ni}^1 = 1; \beta_{1i}^1 = 0.576, \beta_{2i}^1 = 0.655, \\
 & \beta_{3i}^1 = 0.806, \beta_{4i}^1 = 1.272, \beta_{5i}^1 = 0.771, \beta_{6i}^1 = 0.745; \Psi_{1i}^1 = 1; \\
 & \Psi_{2i}^1 = 2; \Psi_{3i}^1 = 3; \Psi_{4i}^1 = \Psi_{5i}^1 = 4; \Psi_{6i}^1 = 5; \Psi_{ni}^1 = [1 + i \cdot \sqrt{\varepsilon_r}]_m)
 \end{aligned}$$

According to formulas (13) and (14), \mathbf{f}_{ni}^1 and their adjacent ratio δ_{ni}^1 of $\mathbf{K}_4\mathbf{S}_1$ are calculated and the results are tabulated in Table 5.

As shown in Table 5, calculated \mathbf{f}_{ni}^1 is very approximate to simulated \mathbf{f}_{ni}^1 and the relative error is less than 5%. So, the supposition that $\mathbf{K}_4\mathbf{S}_1$ KSSG behaves like a half-wavelength dipole in multi-bands is reasonable and accurate. It also clearly revealed that adjacent ratio δ_{ni}^1 is very close to the fractal ratio $\tau^{-1} = 2$ of $\mathbf{K}_0\mathbf{S}_1$ in low frequency and approaches to fractal ratio $\beta_{ni}^1 \cdot \chi^{\frac{1-\Psi_{ni}^1}{\sqrt{\varepsilon_r}}} = \beta_{ni}^1 \cdot \left(\frac{2 \cdot \alpha}{\alpha-1}\right)^{\frac{\Psi_{ni}^1-1}{\sqrt{\varepsilon_r}}}$ of $\mathbf{K}_4\mathbf{S}_0$ in high frequency.

4. CONCLUSION

The monofractals Sierpinski Gasket and Koch-like curve have coalesced into one multifractal in manner of main-minor, forming so called Koch-like sided Sierpinski Gasket multifractal dipole $\mathbf{K}_i\mathbf{S}_j$ KSSG. It has been investigated in free space without feedline for unveiling multifractal traits by simulation with Ansoft HFSSTM v.13. Then a pragmatic multifractal dipole $\mathbf{K}_4\mathbf{S}_1$ KSSG with CPS feeding is designed, fabricated and measured. Compared with its monofractal counterparts $\mathbf{K}_0\mathbf{S}_1$ and $\mathbf{K}_4\mathbf{S}_0$, $\mathbf{K}_4\mathbf{S}_1$ KSSG not only manifests more uniform impedances and more prominent size reduction but also reserves their merits and surmounts their demerits simultaneously. It behaviors like the main fractal in low frequency and resembles the minor one in high frequency. The multifractal antenna is closely relevant to its component monofractals' properties and their combinative way. Consistent results are acquired from measurement and simulation of the physical $\mathbf{K}_4\mathbf{S}_1$ KSSG. Six matched bands

with moderate gain (2 dBi–6 dBi) and high efficiency (75%–95%) are obtained within band 1.5 GHz–14 GHz, of which $f_1 = 2.137$ GHz (14.46%), $f_2 = 4.103$ GHz (9.12%), $f_3 = 5.596$ GHz (3.22%) are generally useful. All the bands are almost omnidirectional or quasi-omnidirectional in H -plane ($\Phi = 0^\circ$, XOZ) and doughnut-shaped or dented doughnut-shaped in E -plane ($\Phi = 90^\circ$, YOZ or $\Theta = 90^\circ$, XOY), which denotes better gain patterns and higher gains than that of [19–22] at f_1 , f_2 , and f_3 respectively. So it is attractive to PCS, IMT-2000, UMTS, WLAN, WiFi, WiMAX and other wireless multiband communication systems.

Multifractal antenna is not simply combined with several different monofractals as in [20] and it has brought forth significant advantages over its monofractal counterparts, such as multiband with multiple frequency ratios, further dimension shrinkage and directivity enhancement. Therefore, it deserves to be ulteriorly explored and developed.

ACKNOWLEDGMENT

The authors were grateful to Qinfang Li from Suzhou R&D Center of Huizhou Speed Communication Technology Co. Ltd. for antenna measurement.

REFERENCES

1. Cohen, N., “Fractal antennas: Part 1,” *Communications Quarterly*, 7–22, Aug. 1995.
2. Cohen, N., “Fractal antenna applications in wireless telecommunications,” *IEEE Electronics Industries Forum of New England*, 43–49, 1997.
3. Werner, D. H., R. L. Haup, and P. L. Werner, “Fractal antenna engineering: The theory and design of fractal antenna arrays,” *IEEE Antennas and Propagation Magazine*, Vol. 41, No. 5, 37–58, Oct. 1999.
4. Kaur, J., S. Singh, and A. Kansal, “Multiband behavior of Sierpinski fractal antenna,” *Res. J. Inform. Technol.*, Vol. 3, No. 1, 35–43, 2011.
5. Sinha, S. N. and M. Jain, “A self-affine fractal multiband antenna,” *IEEE Antennas and Wireless Propagation Letters*, Vol. 6, 110–112, 2007.

6. Rathee, D. and J. Ashraf, "CPW-fed Sierpinski fractal monopole antenna with varying scale factor," *International Journal of Electronics Engineering*, Vol. 3, No. 1, 77–80, 2011.
7. Anguera, J., C. Puente, C. Borja, and J. Soler, "Fractal-shaped antennas: A review," *Wiley Encyclopedia of RF and Microwave Engineering*, Vol. 2, 1620–1635, 2005.
8. Ying, L., S. X. Gong, and D. M. Fu, "The advances in development of fractal antennas," *Chinese Journal of Radio Science*, Vol. 17, No. 1, Feb. 2002.
9. Mandelbrot, B. B., *The Fractal Geometry of Nature*, 2nd edition, W. H. Freeman, New York, 1983.
10. Falconer, K., *Fractal Geometry: Mathematical Foundations and Applications*, 2nd edition, John Wiley & Son, Inc., New York, 2003.
11. Khan, S. N., J. Hu, J. Xiong, and S. He, "Circular fractal monopole antenna for low VSWR UWB applications," *Progress In Electromagnetics Research Letters*, Vol. 1, 19–25, 2008.
12. Puente, C., J. Romeu, R. Pous, and A. Cardama, "On the behavior of the Sierpinski multiband fractal antenna," *IEEE Trans. on Antennas and Propag.*, Vol. 46, 517–524, Apr. 1998.
13. Rosu, I., "Small antennas for high frequencies," <http://www.qsl.n-et/va3iul/>
14. Serkan Basat, S., S. Bhattacharya, and L. Yang, "Design of a novel high-efficiency UHF RFID antenna on flexible LCP substrate with high read-range capability," *IEEE Antennas and Propagation Society International Symposium*, Vol. 7, No. 9, 1031–1034, Jul. 2006.
15. Heldring, A., E. Ubeda, and J. M. Rius, "Efficient computation of the effect of wire ends in thin wire analysis," *IEEE Trans. on Antennas and Propag.*, Vol. 54, No. 10, 3034–3037, Oct. 2006.
16. Hwang, K. C., "A modified Sierpinski fractal antenna for multiband application," *IEEE Antennas and Wireless Propagation Letters*, Vol. 6, 2007.
17. Aneesh Kumar, S. and T. K. Sreeja, "A modified fractal antenna for multiband applications," *IEEE International Conference on Communication, Control and Computing Technologies (ICCCCT)*, Vol. 10, 47–51, 2010.
18. Baliarda, C. P., J. Romeu, and A. Cardama, "The koch monopole: A small fractal antenna," *IEEE Trans. on Antennas and Propag.*, Vol. 48, No. 11, 1773–1781, Nov. 2000

19. Mahatthanajatuphat, C., S. Saleekaw, and P. Akkaraekthalin, "A rhombic patch monopole antenna with modified Minkowski fractal geometry for UMTS, WLAN, and mobile WiMAX application," *Progress In Electromagnetics Research*, Vol. 89, 57–74, 2009.
20. Lizzi, L. and G. Oliveri, "Hybrid design of a fractal-shaped GSM/UMTS antenna," *Journal of Electromagnetic Waves and Applications*, Vol. 24, No. 5–6, 707–719, 2010.
21. Li, C.-M., K. Wang, and C.-K. Chen, "Small Tri-band monopole antenna for WIMAX/WLAN applications," *Journal of Electromagnetic Waves and Applications*, Vol. 25, No. 8–9, 1297–1307, 2011.
22. He, K., R.-X. Wang, Y.-F. Wang, and B.-H. Sun, "Compact Tri-band claw-shaped monopole antenna for WLAN/WIMAX applications," *Journal of Electromagnetic Waves and Applications*, Vol. 25, No 5–6, 869–877, 2011.